



HAL
open science

Atomistic to continuum mechanics description of crystal defects with dislocation density fields: application to dislocations and grain boundaries

Houssam Kharouji, Lucile Dezerald, Pierre Hirel, Philippe Carrez, Patrick Cordier, Vincent Taupin, Julien Guéno

► To cite this version:

Houssam Kharouji, Lucile Dezerald, Pierre Hirel, Philippe Carrez, Patrick Cordier, et al.. Atomistic to continuum mechanics description of crystal defects with dislocation density fields: application to dislocations and grain boundaries. *International Journal of Plasticity*, 2024, 177, pp.103990. 10.1016/j.ijplas.2024.103990 . hal-04471501v3

HAL Id: hal-04471501

<https://hal.univ-lorraine.fr/hal-04471501v3>

Submitted on 1 May 2024 (v3), last revised 21 May 2024 (v4)

HAL is a multi-disciplinary open access archive for the deposit and dissemination of scientific research documents, whether they are published or not. The documents may come from teaching and research institutions in France or abroad, or from public or private research centers.

L'archive ouverte pluridisciplinaire **HAL**, est destinée au dépôt et à la diffusion de documents scientifiques de niveau recherche, publiés ou non, émanant des établissements d'enseignement et de recherche français ou étrangers, des laboratoires publics ou privés.

Atomistic to continuum mechanics description of crystal defects with dislocation density fields: application to dislocations and grain boundaries

Houssam Kharouji^a, Lucile Dezerald^b, Pierre Hirel^c, Philippe Carrez^c, Patrick Cordier^{c,d}, Vincent Taupin^a, Julien Guénoles^{a,*}

^aUniversité de Lorraine, CNRS, Arts et Métiers, LEM3, F-57070 Metz, France

^bInstitut Jean Lamour, CNRS UMR 7189, Université de Lorraine, F-54000 Nancy, France

^cUniversité de Lille, CNRS, INRAE, Centrale Lille, UMET, F-59000 Lille, France

^dInstitut Universitaire de France, F-75005 Paris, France

Abstract

The atomic structure of crystal defects such as dislocations, grain or phase boundaries, control these defects' properties: their mobility, ability to cross-slip, or solute segregation. These crystal defects can be conveniently studied by atomistic simulations and one then needs to transfer relevant information at the upper scale to model microstructures containing a large number of defects, e.g., a polycrystal. Here, we propose an atomistic to continuum mechanics crossover method that (i) represents the atomic structure of dislocations cores by an appropriate Nye dislocation density tensor field and (ii), captures quantitatively the short and long range mechanical fields of defects. For (i), we propose a modified and improved interpolation method based on the original work by Hartley and Mishin. For (ii), we use a field dislocation mechanics framework that rigorously calculates / evaluates the mechanical fields associated with any Nye dislocation density distribution. The transfer method relies on molecular static calculations using two energetic models - ab-initio for screw dislocation core simulations in tungsten, and EAM potential for low and large angle grain boundaries in copper. Our findings demonstrate the effectiveness of the proposed approach in reconstructing the Burgers vector, and continuous strain and rotation fields. The framework is further applied to analyze the elastic interactions between extrinsic edge dislocations and a low angle grain boundary in copper.

Keywords: dislocations, grain boundaries, Nye tensor, Ab-Initio, Molecular Statics, Field Dislocation Mechanics.

1. Introduction

1 Crystal defects, in particular dislocations and grain boundaries (GBs), are well known to control the mechanical
2 properties of crystalline materials. A thorough understanding of these defects is essential for designing materials with
3 mechanical properties tailored for a wide range of applications [1]. Dislocation and GB physics is a multidisciplinary
4 field that investigates the behavior and properties of defects across a broad spectrum of scales, from the atomic-level
5 where, for instance, the dislocation core involves a few atoms only, up to the scale of polycrystals where billions of
6 dislocation lines interact with each others and with GBs. At the atomic scale, Molecular Dynamics/Statics (MD/MS)
7 simulations are widely used to model the fundamental structures and properties of dislocations or GBs. These simu-
8 lations provide detailed and quantitative insights on defected atomic configurations, energies, mobilities, etc. [2, 3].
9 They are also widely used to predict the interactions between dislocations and grain boundaries, and discern con-
10 figurations that facilitate dislocation absorption or transmission through grain boundaries in metallic materials [4].
11 Nonetheless, atomistic simulations are usually limited to small time and size scales, typically of the order of few
12 nanoseconds and tens of nanometers. As such, multiscale efforts are needed to extract relevant physical and mechani-
13 cal information from atomistic simulations, and incorporate it in larger scale models, in order to simulate realistic and
14 statistically meaningful microstructures. Such larger scale modelling approaches are discrete dislocation dynamics

*Corresponding author

Email address: julien.guenole@univ-lorraine.fr (Julien Guénoles)

15 [5, 6], phase field models [7, 8], or continuum mechanics based crystal defect models [9].

16
17 Continuum mechanics approaches are well suited for tracking the evolution of mechanical fields and defected
18 microstructures (elastic/plastic deformation, internal stresses, dislocation densities etc.) at the mesoscale, i.e., at the
19 scale of grains. Frank and Bilby were pioneers in the development of such fundamental theories for mechanically
20 representing the structure of grain and phase boundaries [10, 11]. The continuous approach they proposed describes
21 the interface as a dislocation surface density, more precisely by a Burgers vector density, that accommodates the in-
22 compatibility of elastic transformation at the interface [11]. This model was later adopted by Read and Shockley
23 to establish a correlation between the excess energy of GBs and their misorientation angle [12]. Recently, this model has
24 seen extensions to more general grain boundaries. It was shown that a link between misorientation, Burgers vector
25 content of grain boundaries, and GB excess energy, can be established for a broad spectrum of misorientations and
26 GB types using a generalized Read and Shockley model [13]. The Frank and Bilby model has also been success-
27 fully applied to investigate the migration of tilt GBs in a mean-field micromechanical framework [14]. In a similar
28 context, phase field approaches have demonstrated their ability to study various aspects of crystal elasticity [15], dis-
29 location mobility [16], and deformation twinning in crystalline materials [17]. Phase field models can be enriched by
30 incorporating information from atomistic simulations. For instance, stacking fault energies as obtained from density
31 functional theory (DFT) calculations can be introduced, which allows to model the dissociated structures and mobility
32 of dislocation cores [18].

33
34 The field dislocation mechanics (FDM) model considered in the present work is a somewhat alternative to disloca-
35 tion phase field models at small scales [19]. This approach provides a continuous representation of dislocation cores
36 using an appropriate distribution of dislocation density. It relies on the Nye dislocation density tensor [20], the Kröner
37 incompatibility equation [21], and the dislocation density transport equation [22]. One of the primary advantages of
38 this model is its ability to provide a fully continuous description of crystalline defects using Nye dislocation densities,
39 which enables to model dislocation core structures [23]. The presence of a Nye dislocation density is linked to an
40 incompatible elastic distortion and generates internal stresses. Although the FDM approach can be applied to disloca-
41 tions and grain boundaries, the introduction of disclination fields [24] was proposed to offer an alternative description
42 of such grain boundaries. This model has been successfully applied to tilt GBs [25] and twist interfaces [26]. It
43 notably enables the reproduction of structural units that compose grain boundaries, their excess energy [27] and their
44 migration kinematics [28]. Disclination and/or dislocation density approaches thus allow for the substitution of the
45 atomic structure of defects (such as dislocations and interfaces) for an equivalent representation using defect den-
46 sities, thereby enabling their incorporation into a continuum mechanics framework for upscaling. In addition to being
47 predictive, FDM has previously been compared to analytical solutions, in the case of single dislocations, dislocations
48 near pores and inclusions [29, 30]. Additionally, other dislocation models using gradient elasticity to regularize sin-
49 gularities at the dislocation cores were validated by comparison with molecular statics [31].

50
51 Based on the framework presented above, we have developed a novel method for an atomistic to continuum me-
52 chanics crossover with the objective of capturing the core structure and the continuous mechanical fields of various
53 crystal defects, including dislocations and grain boundaries. We restrict ourselves to field dislocation mechanics here,
54 but the approach can be extended to incorporate disclination fields. Our approach thus involves the description of
55 the atomic structure of crystal defect cores in terms of an equivalent Nye dislocation density. The first stage entails
56 computing the per-atom elastic distortion field from atomistic simulations, the incompatible part of which yields the
57 associated Nye dislocation density. For this task, we are using the Hartley Mishin algorithm [32] that provides the
58 inverse elastic transformation (also called correspondence tensor) as well as the Nye density on each atom in an
59 atomistic configuration. For the second stage, we explore the appropriate metrics, whether it be the per-atom inverse
60 elastic transformation or directly the per-atom Nye tensor, to perform our transition from atomistic data to our contin-
61 uum mechanics FDM model. More precisely, as our FDM model field equations are numerically approximated on a
62 regular fast Fourier transform (FFT) grid, we try different interpolations of atomistic data (transformation or Nye ten-
63 sors) onto the FFT grid and compare with atomistic data in terms of Burgers vector and short/long range mechanical
64 fields (elastic strains and rotations). We assess our atomistic to continuum mechanics crossover by the ability of the
65 atomistic-aided FDM to predict the elastic fields of different defects. Defects include screw dislocations dipoles, edge
66 dislocations array and structural units in high angle tilt grain boundaries.

67
68 The structure of this paper can be summarized as follows. First, we provide an initial overview of the atom-
69 istic methods employed for simulating crystal defects (Section 2). This includes Density Functional Theory (DFT)
70 methods to model $1/2[1\ 1\ 1]$ screw dislocation dipoles in tungsten and Molecular Statics (MS) for producing high and
71 low-angle tilt grain boundaries in copper. In our study, the choice to employ distinct atomistic scale simulation meth-
72 ods for tungsten and copper stems from their difference in terms of crystal structures and mechanical properties and
73 response. Ab-initio simulations accurately capture screw dislocation with cores in BCC Fe by considering the elec-
74 tronic effects, but are computationally intensive. For larger scale simulations, molecular statics using semi-empirical
75 potentials offers a computationally efficient alternative, yet sufficiently accurate. Following this, a brief overview of
76 dislocation mechanics allows us to introduce the Hartley and Mishin algorithm used to compute the per-atom lattice
77 correspondence and Nye tensors. The latter part of Section 2 is devoted to elucidating the method employed for
78 transitioning from atomistic data to our continuous mechanical model. Section 3 is dedicated to applications of the
79 crossover method, where we systematically assess the ability of FDM to reproduce the Burgers vector of defects and
80 their mechanical fields. The final part of Section 3 is focused on applying the transfer method to investigate the in-
81 teractions between extrinsic edge dislocations and a low angle tilt grain boundary. Section 4 concludes our study and
82 presents further directions.

83 2. Methods

84 2.1. Numerical simulation methods

85 2.1.1. Atomistic approaches

86 Ab-initio calculations based on the density functional theory (DFT) were performed to simulate the core structure
87 of $1/2[1\ 1\ 1]$ screw dislocations in body-centered cubic (BCC) tungsten. All computations were carried out using
88 the Vienna ab-initio simulation package (VASP) [33]. The exchange-correlation interactions were described using
89 the Generalized Gradient Approximation (GGA) with the Perdew-Burke-Ernzerhof (PBE) parametrization. A screw
90 dislocation dipole is inserted within a supercell containing 135 atoms with three-dimensional (3D) periodic boundary
91 conditions using periodicity vectors $\vec{C}_1 = 5/2[1\bar{2}1] + 9/2[\bar{1}01]$, $\vec{C}_2 = 5/2[1\bar{2}1] - 9/2[\bar{1}01]$, and $\vec{C}_3 = 1/2[111] = \vec{b}$
92 as presented in the recent work of Bienvenu et al. [34][35][36] (See Figure S1 in Supplementary Material). We set
93 a kinetic energy cutoff of 400 eV for the plane-wave basis and convergence criterion of 0.05 eV/Å on the forces for
94 ionic relaxations.

95
96 To simulate symmetric tilt GBs in face-centered cubic (FCC) copper, we employed the Molecular Dynamics
97 LAMMPS code [37]. The atomic interactions were modeled using the embedded atom method (EAM) potential of
98 Mishin et al [38] for Cu. This potential accurately predicts key physical properties of Cu, including the lattice param-
99 eter, cohesive energy, vacancy formation energy, GB excess energies and elastic stiffness moduli. In this study, we
100 consider the low-angle grain boundary (LAGB) $\Sigma 365(27\bar{1}0)[0\ 0\ 1]4.24^\circ$ and the high-angle grain boundary (HAGB)
101 $\Sigma 5(3\ 1\ 0)[1\ 0\ 0]36.8^\circ$. Figure S2 (supplementary material) illustrates the simulation boxes for each of these GBs. Note
102 that each computational cell contains two opposite grain boundaries because of periodic boundary conditions. The
103 simulation cell dimensions for LAGB and HAGB are $(137 \times 252 \times 3.615 \text{ \AA}^3)$ and $(293 \times 391 \times 3.615 \text{ \AA}^3)$, respectively.
104 These dimensions are sufficiently large to prevent any significant interaction between the two opposite grain bound-
105 aries. Molecular Statics (MS) calculations were performed to determine the minimum energy configuration of each
106 grain boundary. The standard simulation methodology includes rigid body translation of rotated grains, application
107 of atom deletion criteria and the use of the conjugate gradient method for relaxing the initial atomic structures. The
108 details of this methodology were extensively described by Tschopp et al. [39].

109 2.1.2. Continuum mechanics approach: Field Dislocation Mechanics

110 We provide here a brief overview of the FDM model with the most important equations, more details about the
111 model can be found in reference [19]. We consider the elastic deformation of a body containing dislocation lines. The
112 presence of dislocations will be the source of elastic deformation and internal stresses. We first consider a general fi-
113 nite deformation setting and we then simplify into a small strain approximation. For simplicity, let us consider a body
114 containing one dislocation line. The model begins by relating the incompatibility of the elastic transformation tensor

115 to the Burgers vector. Let us consider two material configurations denoted as the reference configuration and the de-
 116 formed configuration, distinguished by their position vectors \mathbf{X} and \mathbf{x} , respectively. The reference system corresponds
 117 to a continuous crystal (without cracks or voids) and without deformation. The deformed material configuration is
 118 obtained by applying to the reference configuration the transformation $\mathbf{F} = \partial\mathbf{x}/\partial\mathbf{X}$. The deformation gradient tensor \mathbf{F}
 119 is multiplicatively decomposed into plastic \mathbf{F}_p and an elastic \mathbf{F}_e tensors, $\mathbf{F} = \mathbf{F}_e \cdot \mathbf{F}_p$. Both tensors contain an incom-
 120 patible non-gradient part, reflecting the elastic and plastic discontinuity due to a non-zero Burgers vector. A possible
 121 measure of this incompatibility is precisely the Burgers vector. The Burgers vector \mathbf{b} is defined as the integral of \mathbf{F}_e^{-1}
 122 along a closed circuit (C) around the dislocation line and is written as follows:

$$\mathbf{b} = - \oint_C \mathbf{F}_e^{-1} \cdot d\mathbf{x}. \quad (1)$$

123 In the above equation, the Burgers vector is measured in the intermediate, or plastic, configuration. If \mathbf{b} equals
 124 zero, it indicates compatibility of the elastic deformation. Conversely, when \mathbf{b} is non-zero, there is incompatibility.
 125 By applying Stokes' theorem to equation (1), we derive:

$$\mathbf{b} = - \iint_S \mathbf{curl}(\mathbf{F}_e^{-1}) \cdot \mathbf{n} dS, \quad (2)$$

126 where S is the surface, with the unit normal \mathbf{n} , bounded by the Burgers circuit. From another point of view now,
 127 the Burgers vectors can be geometrically described through a second-order tensor known as the dislocation density
 128 tensor or so-called Nye tensor α defined as [20]:

$$\mathbf{b} = \iint_S \alpha \cdot \mathbf{n} dS. \quad (3)$$

129 The tensor α has components $\alpha_{ij} = b_i t_j$ in the Cartesian coordinate system, where the density b_i is the length
 130 of Burgers vector in direction i per unit surface and t_j is the unit dislocation line vector component in direction j .
 131 This means that the diagonal terms of the Nye tensor α represent screw dislocations whereas the non-diagonal terms
 132 represents edge dislocations. By identifying the two equations above, we obtain a non-integral expression that relates
 133 the inverse elastic transformation tensor to the Nye tensor:

$$\alpha = -\mathbf{curl}(\mathbf{F}_e^{-1}). \quad (4)$$

134 In a small strain framework now, the inverse of the elastic transformation tensor \mathbf{F}_e^{-1} is related to the elastic
 135 distortion \mathbf{U}_e by $\mathbf{F}_e^{-1} = \mathbf{I} - \mathbf{U}_e$, where \mathbf{I} is the second-order identity tensor. The equation (4) can be rewritten as:

$$\alpha = \mathbf{curl}(\mathbf{U}_e). \quad (5)$$

136 Following the work by Acharya [19], we decompose the elastic distortion into an incompatible non-gradient,
 137 curl part \mathbf{U}_e^\perp , and a compatible, curl-free part \mathbf{U}_e^\parallel , which is a gradient. We therefore apply the Stokes Helmholtz
 138 decomposition:

$$\mathbf{U}_e = \mathbf{U}_e^\perp + \mathbf{U}_e^\parallel = \mathbf{curl}\chi + \mathbf{grad}\mathbf{w}. \quad (6)$$

139 By applying the \mathbf{curl} operator to equation (6), we extract the incompatible elastic distortion, such that we have:

$$\alpha = \mathbf{curl}(\mathbf{U}_e^\perp). \quad (7)$$

140 To obtain a unique and purely rotational solution to the above equation, we must also satisfy $\mathbf{div} \mathbf{U}_e^\perp = 0$. By using
 141 the identity $\mathbf{curl}(\mathbf{curl} \mathbf{A}) = \mathbf{grad}(\mathbf{div} \mathbf{A}) - \mathbf{div}(\mathbf{grad} \mathbf{A})$, the incompatible elastic distortion is given as the solution of
 142 the following Poisson-type equation:

$$\mathbf{div}(\mathbf{grad} \mathbf{U}_e^\perp) = \Delta \mathbf{U}_e^\perp = -\mathbf{curl}(\alpha). \quad (8)$$

143 Equation (8) is solved through a computationally efficient numerical spectral method based on fast Fourier trans-
 144 form (FFT) algorithms, as detailed by Djaka et al. [40]. In order to know the total elastic distortion, we need to

Table 1: Elastic properties predicted for Tungsten with our DFT calculations and via EAM potential for copper. The elastic constants in tungsten were computed within a cell with 1 atom using a $34 \times 34 \times 34$ k-point mesh .

	C_{11} (GPa)	C_{12} (GPa)	C_{44} (GPa)
Tungsten	514.46	203.91	142.4
Copper	169.9	122.6	76.2

145 determine the compatible part, which serves to satisfy the stress equilibrium. Let us call \mathbf{T} the symmetric Cauchy
 146 stress tensor and \mathbf{C} the fourth order elasticity tensor. In the present study, we will use the elastic moduli obtained
 147 from Ab-initio simulations for the screw dislocation in tungsten, whereas for the GBs in copper, we employ the elastic
 148 constants predicted by the Mishin EAM potential [38]. The elastic constants were calculated in the standard basis of
 149 the BCC and FCC structures (see table (1)). The stress tensor reads:

$$\mathbf{T} = \mathbf{C}:\mathbf{U}_e = \mathbf{C} : (\mathbf{U}_e^\perp + \mathbf{U}_e^\parallel). \quad (9)$$

150 and must satisfy the equilibrium equation $\mathbf{div} \mathbf{T} = 0$ in the absence of inertia effects. Finally, using the definition
 151 of \mathbf{U}_e in equation (6), the stress equilibrium equation can be rewritten as:

$$\mathbf{div} (\mathbf{C} : \mathbf{grad} \mathbf{w}) + \mathbf{f}^\perp = 0, \quad (10)$$

152 where $\mathbf{f}^\perp = \mathbf{div}(\mathbf{C}:\mathbf{U}_e^\perp)$ can be interpreted as a volumetric force resulting from the elastic incompatibility associated
 153 with dislocations. The equation (10) is also approximated through a computationally efficient scheme based on FFT
 154 algorithms in the framework of heterogeneous elasticity [40].

155 2.2. Atomistic to continuum mechanics transfer methods

156 2.2.1. Hartley and Mishin original algorithm

157 In this section, we adopt the approach introduced by Hartley and Mishin [32] to calculate the Nye tensor α per
 158 atom. The Nye tensor can be expressed as the curl of lattice correspondence tensor \mathbf{G} , which is the inverse elastic
 159 transformation that maps the position vectors of atoms in a deformed crystal configuration \mathbf{dx} onto those of a perfect
 160 reference crystal configuration \mathbf{dX} by the equation:

$$\mathbf{dX} = \mathbf{G}.\mathbf{dx}. \quad (11)$$

161 To compute the lattice correspondence tensor \mathbf{G} , we define $\mathbf{P}^\gamma (\gamma = \{1, 2, 3, \dots, n\})$ and $\mathbf{Q}^\beta (\beta = \{1, 2, 3, \dots, m\})$ as the
 162 set of position vectors between atom i and all its neighboring atoms (n and m) within a specified cutoff radius R_c
 163 in the perfect configuration and the deformed configuration respectively. It is important to note that the choice of cutoff
 164 radius significantly impacts the \mathbf{G} fields and the Burgers vector calculations. In the systems simulated here, we select a
 165 cutoff distance of $R_c = 0.93a_0$ and $0.86a_0$ for BCC and FCC, respectively. These values correspond to half the distance
 166 between the first and second neighbor shells in the BCC and FCC systems. For each \mathbf{Q}^β we locate the corresponding
 167 \mathbf{P}^γ with the closest angle match. This is achieved by calculating the angular difference between the two vectors, i.e.,
 168 for each \mathbf{Q}^β we seek the \mathbf{P}^γ vector yielding the shortest angle. If there is no \mathbf{P}^γ vector found within a fixed tolerance
 169 θ_{max} , we exclude that \mathbf{Q}^β . However, if a match is found, we compare the lengths of the two \mathbf{Q}^β vectors and retain
 170 the one that is closest in length to \mathbf{P}^γ . According to Hartley and Mishin [32] suggestion, we employed $\theta_{max} = 43^\circ$
 171 for BCC and $\theta_{max} = 27^\circ$ for FCC systems, which closely aligns with half of the angle between the \mathbf{P}^γ vectors. After
 172 the vector rejections, the number of \mathbf{P}^δ and \mathbf{Q}^δ sets, with $\delta = \{1, 2, \dots, s\}$, will be either equal to or less than β and γ . The
 173 lattice correspondence tensor \mathbf{G} is evaluated for a given atom as a least squares solution of the linear matrix equation:

$$\mathbf{Q}.\mathbf{G} = \mathbf{P}, \quad (12)$$

174 where matrices \mathbf{P} and \mathbf{Q} have dimensions of $(s \times 3)$, with each row representing the index of vector (δ) and each
 175 column representing the components of the vectors along the reference Cartesian axes. According to Harley and
 176 Mishin convention, the Nye tensor α can be expressed as function of the lattice correspondence tensor \mathbf{G} by:

$$\alpha = -\text{curl}(\mathbf{G}). \quad (13)$$

177 It is important to highlight that within the Hartley and Mishin approach, the counterpart to the lattice correspon-
 178 dence tensor is represented as the transpose of the elastic transformation inverse in the FDM approach. This means
 179 that:

$$\mathbf{G} = (\mathbf{F}_e^{-1})^T. \quad (14)$$

180 By using the Einstein notation, the Nye tensor in our FDM model is thus expressed in rectangular cartesian
 181 components as:

$$\alpha_{ij} = -\epsilon_{jkl} \frac{\partial G_{il}^T}{\partial x_k}, \quad (15)$$

182 where \mathbf{e} is the Levi-Cevita permutation tensor. In the Hartley and Mishin algorithm, the per-atom Nye tensor is
 183 then estimated through an approximation of spatial derivatives involved in the curl operation. The algorithm has been
 184 recently implemented in available atomistic tools designed for the construction and analysis of large-scale atomic
 185 systems, such as Atomman [41] and Atomsk [42]. Both tools were tested and yielded similar results for the \mathbf{G} and α
 186 per-atom fields. **Notably, the simulation time needed is a few seconds.**

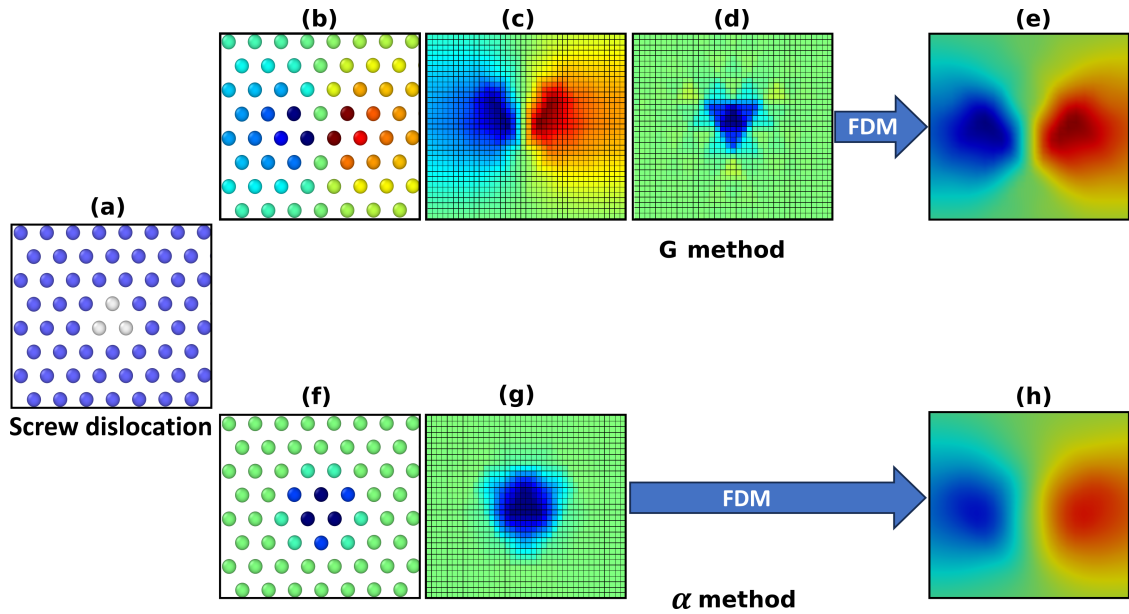


Figure 1: Schematic representation of the atomistic to continuum transfer techniques: (a) Visualization of a $1/2[1 1 1]$ tungsten screw dislocation core in OVITO[43]. The atomistic core structure is colored using common neighbor analysis: Blue atoms represent BCC environment and white atoms indicate a non-BCC environment. The figures (b),(c), (d) and (e) depict the workflow of the G method. (b) The component G_{23} of the per-atom lattice correspondence tensor calculated by Harley and Mishin algorithm. (c) Interpolation G_{23} on the FFT grid. (d) Calculation of the component α_{33} of the Nye tensor on the FFT grid. (e) Visualization of elastic distortion maps obtained from solving the FDM equations. The figures (f),(g) and (h) represent the workflow of the α method. (f) The component α_{33} of the per-atom Nye tensor calculated by Harley and Mishin algorithm. (g) Interpolation of α_{23} on the FFT grid. (h) Visualization of elastic distortion maps obtained from solving the FDM equations.

187

188 2.2.2. Atomistic to continuum transfer

189 In this section, we outline two different approaches employed for using possible atomistic data for a given crystal
 190 defect (dislocations or GBs), as input in the FDM model. We remind that the FDM field equations (8) and (10) are

191 numerically approximated on a regular FFT grid, following [40]. As such, we need to transfer per-atom atomistic
192 (ab-initio or MS) data onto an FFT grid. Atomistic, per-atom data fields, can be either \mathbf{G} or directly α . As illustrated
193 in Fig. 1, the first approach, denoted G method, involves the computation of the per-atom lattice correspondence
194 tensor using the Hartley and Mishin algorithm (Fig.1b). The tensor components are then interpolated onto the FFT
195 grid (Fig.1c), on which we can then estimate the curl to determine the Nye tensor using a finite difference approxi-
196 mation (Fig.1d). From this, we can solve the FDM equations to obtain the continuous elastic distortion field Fig.1e.
197 The second approach, denoted α method, involves the calculation of the per-atom Nye tensor using the Hartley and
198 Mishin algorithm (Fig.1f). The components α_{ij} of this tensor are then directly interpolated on the FFT grid (Fig.1g)
199 and use as input to solve the FDM equations, leading to another continuous elastic distortion field (Fig.1h). Finally,
200 we can compare the continuous elastic distortion fields obtained via both G and α methods to the elastic per-atom
201 elastic fields obtained using the Hartley and Mishin algorithm. It is worth noting that we evaluated various interpo-
202 lation methods, including spline, cubic, and nearest neighbor interpolations. It appeared that linear interpolation was
203 perfectly adequate (see Figures S5 and S6 in Supplementary Material). In terms of computation time the transfer
204 method, including interpolation and the resolution of the Field dislocation mechanics (FDM) equations, is not com-
205 putationally expensive. The simulation time is a few seconds on one processor. However, it is important to note that
206 the atomistic simulations remain computationally expensive. We have provided a detailed table in the supplementary
207 material, showing the simulation time and the number of CPUs required for each defect and for each Fast Fourier
208 Transform (FFT) grid resolution. It is thus computationally very cheap to build an entire database of defects, provid-
209 ing the atomistic configurations of defects are already available and a fully automated framework has been designed.
210 As an example of such available data, the grain boundaries dataset from Tschopp et al. [39]

211 3. Results and discussion

212 3.1. Benchmark test

213 The transfer methods introduced in section 2.2.2 are first assessed by considering $1/2[1\ 1\ 1]$ screw dislocations
214 in tungsten. Figure 2 depicts the influence of FFT grid resolution on the Nye component α_{33} distribution using G
215 and α methods. For the finest resolution tested ($0.5\ \text{\AA}$, Fig. 2 (b) and (c)), both methods successfully capture the
216 screw density distribution obtained with DFT (Fig. 2 (a)). However, the three-fold symmetry of the screw dislocation
217 core is only captured by the G method at $0.5\ \text{\AA}$ resolution (Fig. 2 (b)). It is also with this method and resolution that
218 we manage to obtain the most compact core, which is a specific feature of screw dislocation cores in BCC metals.
219 Fig. 2 (c) and (e) show that a $2\ \text{\AA}$ resolution does not reproduce the 3-fold symmetry of the dislocation core, for either
220 method. We have quantitatively evaluated both methods by calculating the error on the magnitude of the Burgers
221 vector relative to the ideal value ($b_{ideal} = 2.762\ \text{\AA}$). Given the Nye tensor definition in equation (3), the Burgers vector
222 is numerically calculated by integrating the Nye tensor over a rectangular grid in a plane normal to the dislocation
223 line. Figure 2 (f) depicts the variation of the error as a function of the FFT grid resolution for both methods.

224

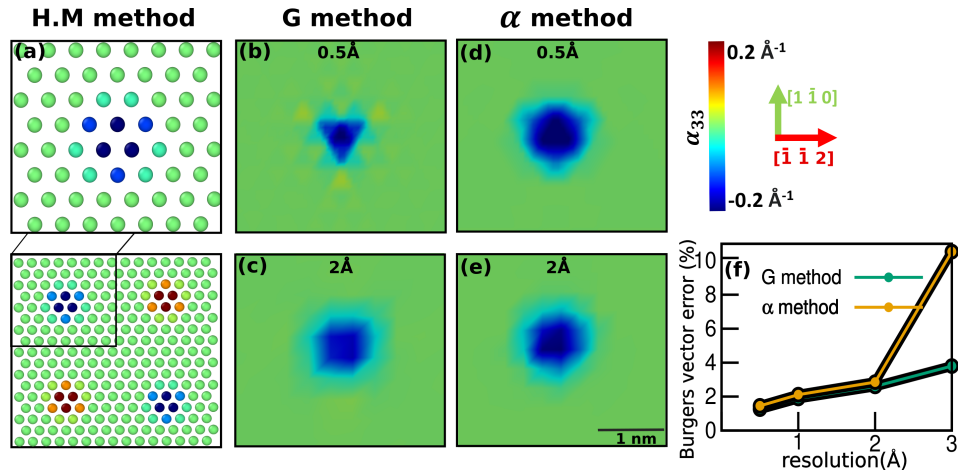


Figure 2: Screw dislocations in tungsten. Effect of FFT grid resolution on Nye dislocation density distributions and Burgers Vector norm error using G and α methods. (a) Visualization of the per-atom component α_{33} of the Nye tensor as obtained from the Hartley-Mishin method applied to the DFT calculations. Red represents positive dislocation density and blue the negative one. (b) and (c): maps illustrating the screw dislocation density distribution obtained using the G method with FFT grid resolutions of 0.5 Å and 2 Å, respectively. (d) and (e) depict screw dislocation density distributions using the α method with 0.5 Å and 2 Å FFT grid resolutions. (f) The variation of the Burgers vector norm error as a function of the grid resolution using the G method (green line) and α method (yellow line).

225 We observe two distinct regions in Fig. 2 (f). For resolutions up to 2 Å, both methods exhibit similar efficiency,
 226 while for resolutions higher than 2 Å, the α method shows noticeable increase in the error percentage. This correlates
 227 with the fact that the core is less compact than expected for higher resolutions. Thereby, when using coarser reso-
 228 lutions, the accurate description of the core is compromised due to the loss of information during interpolation. An
 229 identical procedure was carried out for edge dislocations within LAGB in copper (see Figure S3 in Supplementary
 230 Material) and also showed an increased error percentage for resolutions higher than 0.5 Å, and a loss of core symmetry
 231 for resolutions of 2 Å and more. Consequently, in the following, we consider the resolution of 0.5 Å, which provides
 232 the best description of the dislocation core.

233 3.2. Inspection of Nye dislocation density distributions

234

235 In the following, we compare qualitatively the efficiency of the G and the α methods in terms of Nye dislocation
 236 density distributions for the $1/2[1\ 1\ 1]$ screw dislocations in tungsten (screw densities), LAGB and HAGB in copper
 237 (edge densities). The first column of Figure 3 shows the distribution of the atomic Nye tensor for the three defects
 238 studied. Hartley and Mishin's method can be extended to calculate the Nye tensor within a grain boundary. This is
 239 particularly useful because identifying the ideal reference configuration can be challenging for systems as complex
 240 as grain boundaries, such as multi-phase boundaries. In this study, we opted for the Displacement Shift Complete
 241 (DSC) lattice as our reference system for the grain boundary [44], as it is typically closely aligned with the positions
 242 of the atoms within the GB [45]. In the third row, we examine the atomic Nye tensor of a symmetric tilt HAGB
 243 $\Sigma 5(3\ 1\ 0)[0\ 0\ 1]$ (Figures 3 (c), Fig. 3 (f) and Fig. 3 (i)). This specific system holds considerable importance to assess
 244 our approach as the GB structure is not described by a dislocation array as for LAGB, but by structural units. We
 245 observe that for all defects, the G method results in a highly concentrated Nye edge dislocation density distribution
 246 in each structural unit, whereas the α method produces a spread-out distribution. Interestingly, the result from the
 247 G method for LABG and HAGB suggests that each structural unit can be interpreted as an edge dislocation with an
 248 equivalent Burgers vector $[0\ 1\ 0]$. While dislocation based models are usually said to be limited to low misorientations
 249 ($< 15^\circ$), our results rather suggest they are actually also applicable to HAGBs. Last but not least with the G method,
 250 the edge dislocation core in the LAGB and the structural unit cores in the HAGB have the largest edge dislocation
 251 density at the place where there is no atom (where there is an excess volume). As such, the G method offers a more
 252 appropriate continuous description of the defect cores than the per-atom Nye estimation for such defects. However,

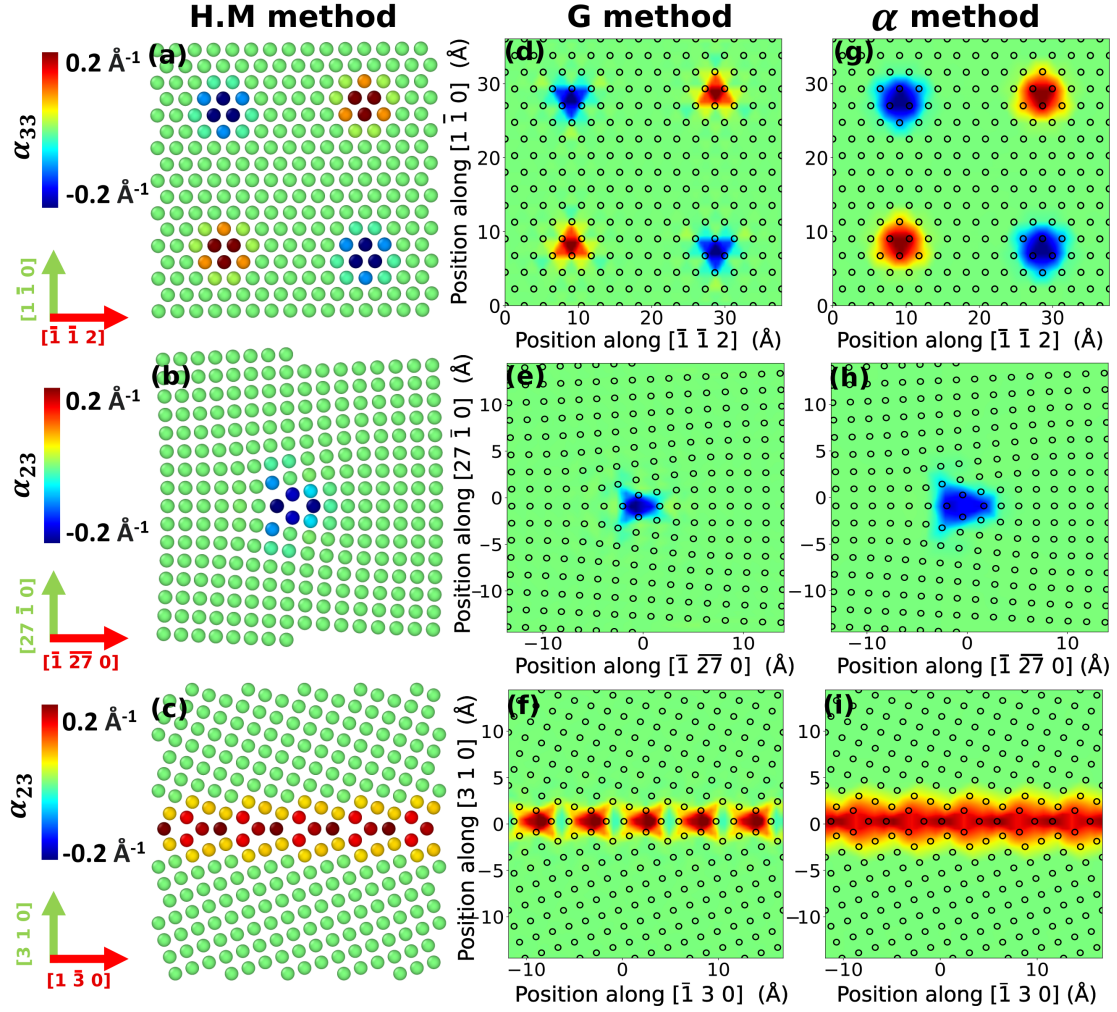


Figure 3: Comparison of Nye dislocation density distributions obtained with the G and α transfer methods using a 0.5 Å FFT grid resolution. (a), (b) and (c) Visualization of the component α_{33} and α_{23} of the Nye tensor for the screw dislocation quadruple in tungsten, structural units within LAGB and HAGB in copper respectively after atomistic relaxation. (d), (e) and (f) Represent maps displaying the screw and edge dislocation densities obtained via the G method. (g), (h) and (i) show the same densities obtained with the α method.

253 we expect certain limitations of the proposed method when dealing with highly disordered grain boundaries where
 254 structural units are indiscernible.

255 3.3. Inspection of elastic fields: strain and rotation

256

257 We will now explore the applicability of the transfer methods in evaluating the elastic strain/rotation fields generated
 258 by the dislocations and GBs. First, the atomic elastic strain field obtained through the lattice correspondence tensor
 259 will be qualitatively compared to the continuous elastic fields obtained from FDM simulations, using input dislocation
 260 densities from the transfer methods. The components of the per-atom strain ε_{ij} can be computed from the lattice
 261 correspondence tensor \mathbf{G} by

$$\varepsilon_{ij} = ((\delta_{ij} - G_{ij}) + (\delta_{ij} - G_{ji}))/2, \quad (16)$$

262 where δ_{ij} is the Kronecker symbol. The figures 4 (a), 4 (b) and 4 (c) represent the distribution of the out-of-plane
 263 shear component ε_{23} of the elastic strain field from a screw dislocations in tungsten. The color scale used in Fig. 4

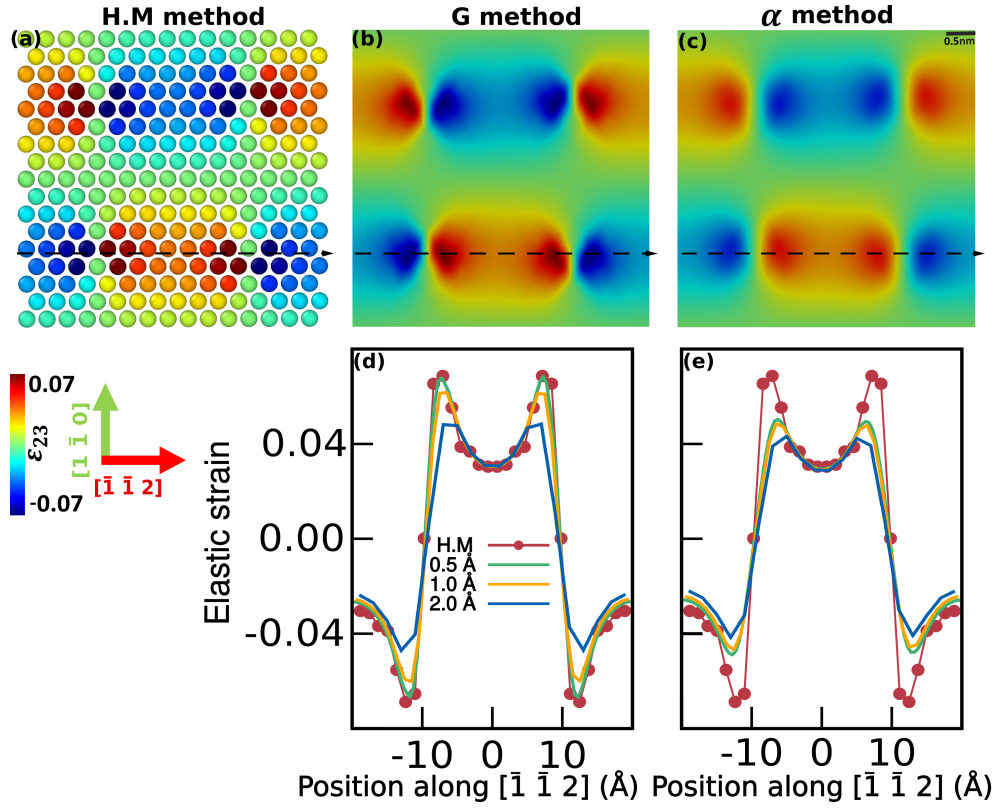


Figure 4: Elastic strain field obtained for screw dislocation quadruple in tungsten with the G and α transfer methods using a 0.5 Å FFT grid resolution and compared to the HM method atomistic result. (a) Visualization of the per-atom strains ϵ_{23} using Hartley and Mishin method. (b) and (c) Maps displaying the elastic strain fields obtained via the G and α methods. The dashed lines indicate the directions for plotting profiles. (d) and (e) represent the elastic strain ϵ_{23} profiles along the $[\bar{1} \bar{1} 2]$ direction obtained with the G and α methods.

264 represents strain ranging from -7 % to +7 %. It is identical for both atomistic and continuous representations.

265 In the case of positive screw dislocations, there is positive shear strain on the left side and a negative shear strain
 266 on the right side of the dislocation core, which qualitatively aligns with the elastic field predicted for a straight
 267 screw dislocation line in isotropic elasticity. As described earlier, the structural units composing the low-angle grain
 268 boundary can be seen as an array of edge dislocations. Figures 5 (a), 5 (b) and 5 (c) exhibit the distribution of the
 269 in-plane shear component ϵ_{12} of the elastic strain field of an isolated dislocation in the LAGB. The field acquired by
 270 both transfer methods closely aligns with the results from atomistic calculations, demonstrating a good agreement
 271 between both approaches. In the case of the screw dislocations and LAGB however, we observe that the G method
 272 much better captures the high strain gradients in the immediate core region of defects, while both methods accurately
 273 capture the relatively smaller strains in regions away from the defect cores.

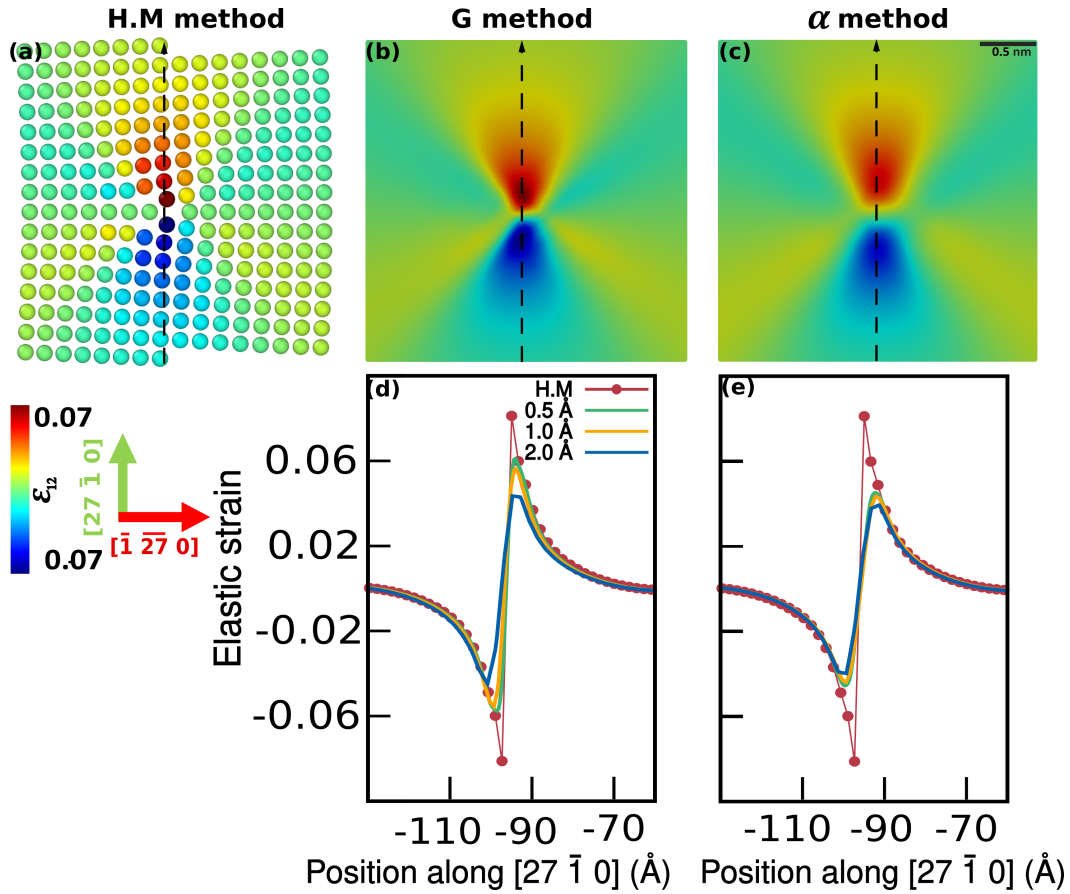


Figure 5: LAGB in copper: Elastic strain field obtained with the G and α transfer methods using a 0.5 Å FFT grid resolution and compared to the HM method atomistic result. (a) Visualization of the per-atom elastic strain ϵ_{23} . (b) and (c) Maps displaying the elastic strain field ϵ_{23} obtained via the G and α methods. The dashed lines indicate the directions for plotting profiles. (d) and (e) represent the elastic strain ϵ_{12} profiles along the $[27 \bar{1} 0]$ direction obtained with the G and α methods.

274 To quantify these observations, we plot the distribution profiles of the elastic fields ϵ_{23} and ϵ_{12} , following the
 275 directions marked with dashed lines on figures 4 and 5 (d). For the screw dislocation cores, figures 4 (d) and 4 (e)
 276 compare the profiles of the atomic strain field (red solid line with symbols) and the continuous strain fields (solid lines)
 277 obtained using the G and α methods respectively, for different FFT grid resolutions. The results show the correct
 278 reproduction of the significant gradient of strain at dislocations core, with the G method and fine resolutions. The
 279 ability to capture these core-level strains is degraded at a resolution of 2 Å. The comparison between the atomistic
 280 and the continuous strain field obtained using the α method reveals that this approach is not as effective as the G
 281 method in capturing the high strain levels near the dislocation core, even when employing the finest resolution. It is
 282 also noteworthy that the resolution has more effect on the G method than on the α method, and that both methods
 283 capture correctly the long-range elastic fields away from the defect cores, whatever the resolution. Similar findings
 284 apply to the case of the LAGB (Figures 5 (d) and 5 (e)). While the G method reproduces almost perfectly the strain
 285 fields at the core of screw dislocations obtained from DFT, it is slightly less efficient to reproduce the elastic fields
 286 observed around the dislocation and structural unit cores within grain boundaries as obtained with semi-empirical
 287 potentials. Figures 6 (d) and 6 (e) show the profiles of the tilt elastic rotation field, describing the grain boundary
 288 misorientation angle along the $[3 1 0]$ direction, using the G and α methods, respectively. Both methods effectively
 289 capture the expected rotation field, the G method providing a slightly better agreement with atomistic results. For the
 290 finest FFT grid resolution, both approaches converge to a misorientation angle of 0.632 radians, corresponding to the
 291 characteristic misorientation of the $\Sigma 5(3 1 0)[0 0 1]$ grain boundary considered in this work.

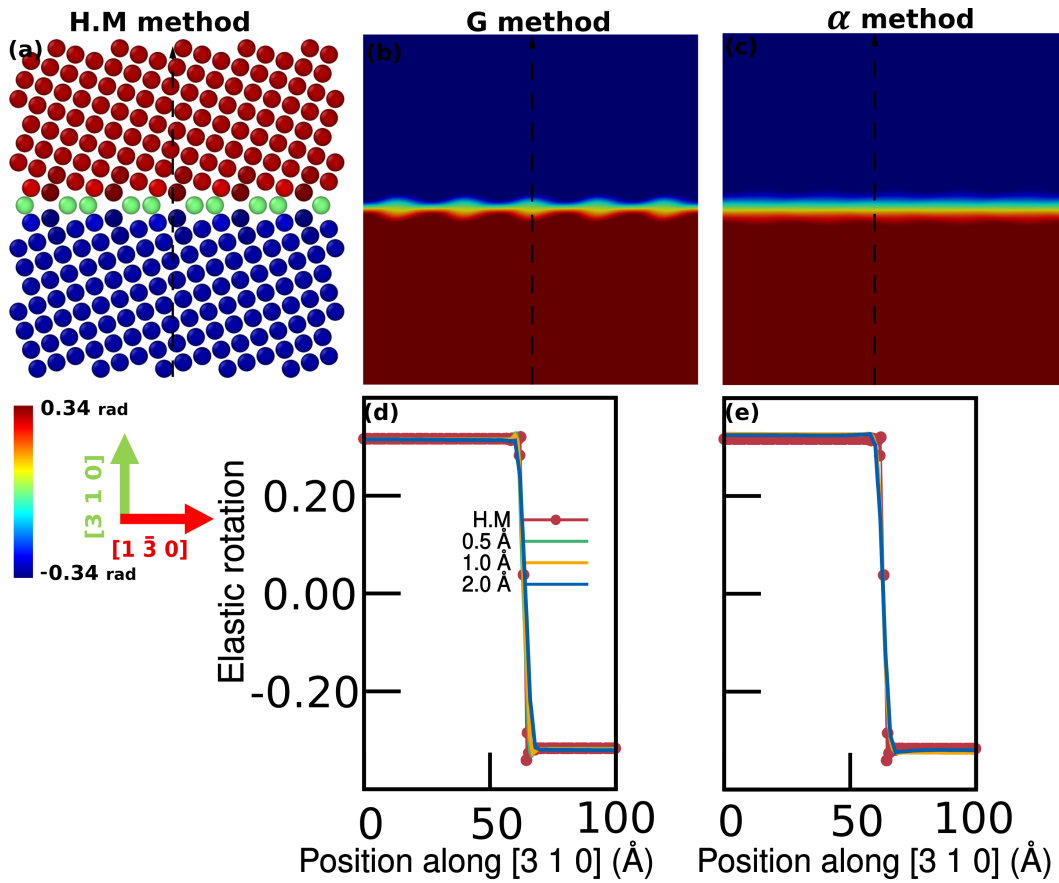


Figure 6: HAGB in copper: Elastic rotation field obtained with the G and α transfer methods using a 0.5 Å FFT grid resolution and compared to the HM method. (a) Visualization of the per-atom elastic rotation. (b) and (c) Maps displaying the rotation field obtained via the G and α methods. The dashed lines indicate the directions for plotting profiles. (d) and (e) represent the tilt rotation profiles along the $[3\ 1\ 0]$ direction obtained with the G and α methods.

292 3.4. Application to dislocation / grain boundary interactions

293 In light of the previous examples, the G method, using a 0.5 Å FFT resolution, demonstrates to be effective
 294 in capturing the short and long range mechanical fields generated by screw dislocations, low and high angle grain
 295 boundaries. The next focus involves the application of the G method to investigate the elastic interactions between
 296 $\Sigma 291(13\bar{1}\bar{1}1)[\bar{1}\bar{1}2]$ symmetric tilt grain boundary and edge extrinsic dislocations in copper. Two molecular static
 297 simulation scenarios were performed. In the first scenario (Figure 7 (a)), the extrinsic dislocation is aligned with an
 298 intrinsic dislocation composing the grain boundary. The two dislocations have opposite sign. In the second scenario
 299 (Figure 7 (d)), the dislocation is shifted by two $\{1\ 1\ 1\}$ planes in such a way that the extrinsic dislocation is aligned
 300 in between two intrinsic dislocation composing the grain boundary. To bring the systems into equilibrium, the FIRE
 301 algorithm [46] is used and the configurations were considered optimized when the norm of the global force vector is
 302 below 10^{-6} eV/Å.

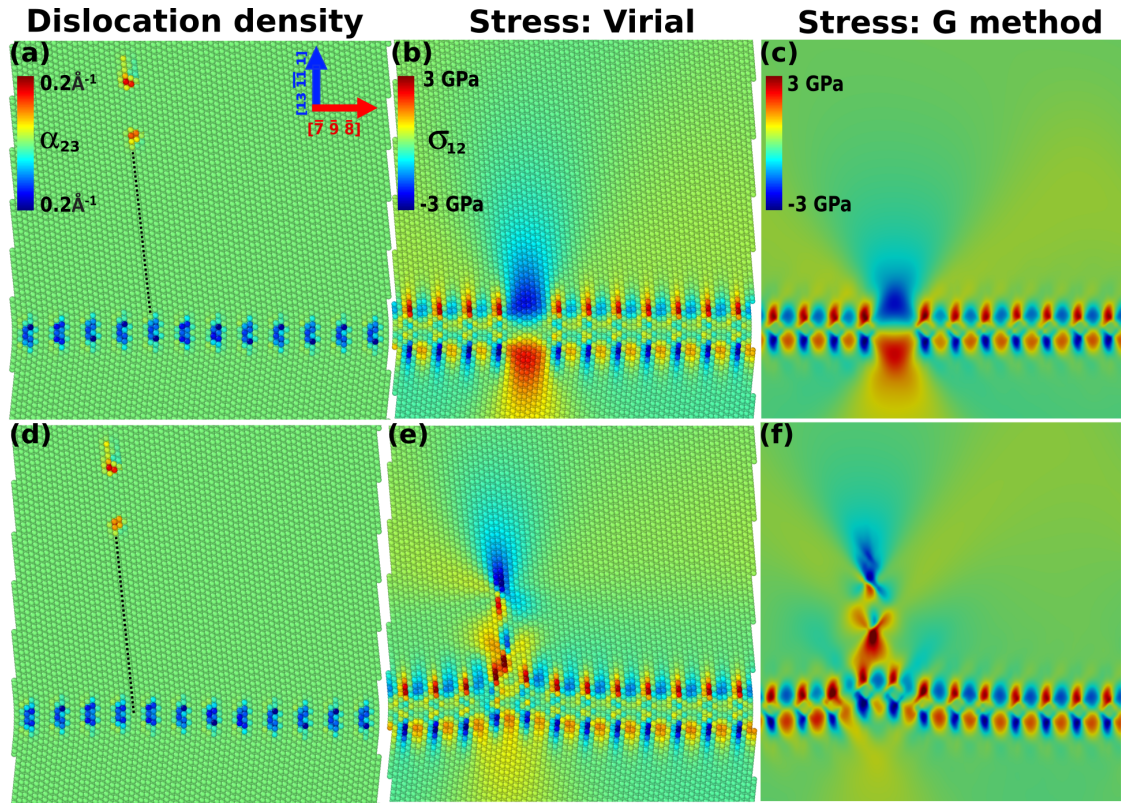


Figure 7: Interaction between an extrinsic edge dislocation and a $\Sigma 291(13\bar{1}\bar{1}1)[\bar{1}\bar{1}2]$ low angle STGB in copper, with two scenarios: the edge dislocation will annihilate with one composing the GB (a,b,c); the edge dislocation will stop nearby the GB (d,e,f). Figures (a,d) show the per-atom Nye dislocation density α_{23} in the initial (unrelaxed) configuration for both scenarios. The presence of two positive α_{23} distributions indicates a dissociation of the extrinsic dislocation into Shockley partials. The dashed black lines indicate the $\{111\}$ glide plane of the extrinsic edge dislocation. In (b,e) is shown the per-atom virial stress σ_{12} of the final (relaxed) configuration, when the edge dislocation has interacted with the GB, for both scenarios. Figures (c,e) show the same stress fields obtained via application of the G method with a 0.5\AA FFT grid resolution.

303 During the minimization process, the extrinsic edge dislocations are dissociated into two Shockley partials. This
304 is illustrated in Figures 7 (a) and 7 (d), where two positive Nye distributions can be seen separated by a specific dis-
305 tance corresponding to the stacking fault separating the two Shockley partials. Figure S4 (in supplementary materials)
306 describes the details of the systems' configuration using the per-atom Nye dislocation density. The Burgers vector
307 norm of dislocations is $b = 2.56\text{\AA}$. This value is calculated by integrating the Nye tensor over a rectangular grid in
308 a plane normal to the dislocation line. The G method is applied to capture the interactions of the elastic stress fields
309 induced by the inserted edge dislocation and the low angle grain boundary, and compared to the virial stress calculated
310 by molecular static simulations. Depending on the initial position of the extrinsic dislocation, two distinct interaction
311 scenarios are observed. Figures 7 (b) and (c) depict the per-atom virial shear stress and that obtained with the G trans-
312 fer method, respectively, illustrating the first interaction scenario. The extrinsic edge dislocation has annihilated
313 with one intrinsic dislocation composing the GB. The grain boundary is indeed described as an array of edge dislocations,
314 where the core of each dislocation undergoes slight dissociation into two Shockley partials. This annihilation results
315 in a local increase in the stress field due to a reduction in the elastic screening between neighboring intrinsic GB
316 dislocations. In the second scenario, the extrinsic dislocation stabilizes near the grain boundary, causing disruption in
317 the dislocation network within the grain boundary and slight migration towards the dislocation (Figures 7 (e) and (f)).
318 The short-range elastic interactions between the extrinsic dislocation and the GB dislocations is rather well captured
319 by the G method in both scenarios. Note that this relaxed configuration is not realistic, as annihilation should likely
320 occur by local climb process. It is not possible here as simulations are performed at 0K. Similarly, we evaluated the
321 interaction between an extrinsic edge dislocation and a $\Sigma 35(\bar{5}31)[112]$ 34.05° high angle grain boundary in copper.

322 The structural units forming the grain boundary, as depicted in Figure S7 (Supplementary Material), are represented
323 by an edge dislocation with highly localized elastic strain fields. Figure S7 (Supplementary Material) compares the
324 stress field obtained by the G method with the Virial stress. We observed that after energy minimization, the edge
325 dislocations glide and stop nearby the grain boundaries, affecting their elastic fields. However, no real interactions
326 (such as dislocation absorption and decomposition) are predicted by this simulation, which somehow resembles that
327 of the low angle grain boundary. To predict more complex interactions, one would need to test other configurations,
328 run simulations with finite temperature and/or applied stress.

329 4. Conclusions and perspectives

330 This paper introduces a new methodology to establish an atomistic to continuum mechanics crossover method,
331 whereby atomic positions in defected regions are used to derive a continuous Nye dislocation density field that is an
332 input in a Field Dislocation Mechanics model. This approach is primarily based on the derivation of the per-atom
333 Nye and lattice correspondence tensors obtained from the Hartley and Mishin method, which we then use as possible
334 inputs on a FFT grid to derive as best as possible the continuous Nye tensor for FDM simulations. The practical
335 outcomes of our research underline the effectiveness of the G method, which relies on interpolating the components
336 of the lattice correspondence tensor as input on the FFT grid. With this method, the FDM model can accurately predict
337 the Burgers vector of defects, as well as the elastic strain and rotation fields near and away from the defect cores, in
338 particular in the case of the screw dislocations simulated by DFT. Note also the efficiency of the FDM model, despite
339 it being formulated within a small strain, linear elastic framework. Another interesting and unexpected result for high
340 angle grain boundaries with structural units closely packed, is that the latter can be described as localized, equivalent,
341 edge dislocations. This approach is thus in favor of dislocation based models for GBs and represents a compelling
342 alternative for modeling high angle grain boundaries without relying on disclination fields [27]. The methodology
343 was extended to investigate the interactive elastic fields between an extrinsic edge dislocations and a low angle grain
344 boundary. It highlights how the stress field due to the presence of the dislocation influences the dislocation network
345 at the grain boundary. We have also tried to simulate a more complex case involving the interaction between edge
346 dislocations and a high-angle tilt grain boundary.

347 Based on our examination of FFT Field Dislocation Mechanics simulations incorporating atomistically informed
348 input dislocation density, we conclude that one major implication of the present work is the following. The per-atom
349 lattice correspondence tensor G is well estimated using the Hartley & Mishin algorithm, which well conserves the
350 incompatibility of G . Such is achieved by directly expressing G as the matrix that maps vectors from the deformed
351 atomic configuration onto the reference configuration. In contrast, extracting atomic displacement fields and then
352 taking their spatial gradients to derive G would lead to a curl-free gradient tensor G , and one would completely lose
353 the incompatibility of G and predict a null dislocation density. By comparing our method “alpha”, where we directly
354 interpolate the per-atom dislocation density, to the “G” method, where we interpolate the per-atom G tensor and
355 then derive the dislocation density with finite differences on a regular grid, we show however that the per-atom Nye
356 dislocation density is less efficiently captured by the Hartley & Mishin algorithm. There are two reasons for this.
357 First, 3D spatial derivatives in the Cartesian frame are not accurately estimated using atomic values and positions.
358 Second and perhaps more importantly, large local dislocation densities in the core regions of defects can be missed
359 because there is no atom in such regions to bear the corresponding dislocation density. This second problem is indeed
360 observed in structural units in our work, where the G-method shows that the largest dislocation density is located at
361 the center of structural units, which contain no atom. As part of the dislocation density is missed, the predicted elastic
362 fields by FDM do not match those from atomistics. The present results thus suggest that the per-atom G tensor is
363 well estimated by the Hartley & Mishin algorithm, but that it is preferable to then derive the dislocation density by
364 interpolating the G tensor on a regular grid. This appears to be true for all benchmark cases studied in this work.

365 A development of our transfer approach could be on polycrystalline materials. While we considered here only
366 (quasi) 2D configurations, our method is intrinsically 3D and can be extended to study interfacial plasticity, i.e.,
367 mechanisms related to grain boundary - dislocation interactions. This would allow considering the presence of initial
368 grain boundary dislocation content and short/long range internal stresses, and the effects on the development of plastic
369 deformation within grains and at/across GBs. An ongoing development of our approach concerns the assessment of
370 strain gradient plasticity models based on GND or Nye dislocation density tensor. Such models add supplementary

371 internal energy functionals based on the Nye tensor to better capture size effects [47] or dislocation transfer mech-
372 anisms at GBs [9], for instance. By applying our method to excess grain boundary energies measured by atomistic
373 simulations for various grain boundaries, it is possible to test different energy functionals proposed in the literature and
374 to quantify the internal characteristic lengths introduced. Furthermore, ongoing efforts are directed towards extending
375 the applicability of our workflow to hexagonal close-packed (HCP) materials.

376 While the method we propose here holds great potential for various defects and structures, we recognize that
377 computing the per-atom Nye tensor may pose challenges in specific cases, particularly with complex structures like
378 phase boundaries or crystal defects in chemically complex materials such as high entropy alloys. Furthermore, the
379 method may encounter limitations when applied to highly disordered grain boundaries, which does not exhibit well
380 defined structural units. Future work may focus on exploring these corner cases and other extensions of the approach,
381 including taking into account dynamic effects.

Competing interests

There are no conflicts to declare.

Acknowledgments

H.K., L.D, V.T. and J.G acknowledge funding from the LabEx DAMAS (Laboratory of Excellence on Design of Alloy Metals for low-mAss Structures). H.K acknowledges financial support from the Région Grand-Est. V.T., L. D. and J.G. acknowledges funding from the French National Research Agency (ANR), Grant ANR-21-CE08-0001 (ATOUM). High Performance Computing resources were provided by the EXPLOR center of the Université de Lorraine and by the GENCI-TGCC (grant Grant 2022-A0120911390). P.H., Ph.C. and P.C. acknowledge funding from the European Research Council (ERC) under the European Union's Horizon 2020 research and innovation programme under grant agreement No 787198 – TimeMan.

References

- [1] N. Bertin, R. B. Sills, W. Cai, *Frontiers in the simulation of dislocations*, *Annual Review of Materials Research* 50 (2020) 437–464.
- [2] C. Xu, X. Tian, W. Jiang, Q. Wang, H. Fan, *Atomistic migration mechanisms of $[12\bar{1}0]$ symmetric tilt grain boundaries in magnesium*, *International Journal of Plasticity* 156 (2022) 103362.
- [3] C. R. Weinberger, G. J. Tucker, *Multiscale materials modeling for nanomechanics* (2016).
- [4] E. Borodin, A. Mayer, M. Y. Gutkin, *Coupled model for grain rotation, dislocation plasticity and grain boundary sliding in fine-grained solids*, *International Journal of Plasticity* 134 (2020).
- [5] H. Espinosa, M. Panico, S. Berbenni, K. Schwarz, *Discrete dislocation dynamics simulations to interpret plasticity size and surface effects in freestanding fcc thin films*, *International Journal of Plasticity* 22 (2006).
- [6] S. Lu, J. Zhao, M. Huang, Z. Li, G. Kang, X. Zhang, *Multiscale discrete dislocation dynamics study of gradient nano-grained materials*, *International Journal of Plasticity* 156 (2022).
- [7] C. Miehe, F. Aldakheel, A. Raina, *Phase field modeling of ductile fracture at finite strains: A variational gradient-extended plasticity-damage theory*, *International Journal of Plasticity* 84 (2016).
- [8] M. Jafari, M. Jamshidian, S. Ziaei-Rad, D. Raabe, F. Roters, *Constitutive modeling of strain induced grain boundary migration via coupling crystal plasticity and phase-field methods*, *International Journal of Plasticity* 99 (2017).
- [9] M. Jebahi, L. Cai, F. Abed-Meraim, *Strain gradient crystal plasticity model based on generalized non-quadratic defect energy and uncoupled dissipation*, *International Journal of Plasticity* 126 (2020).
- [10] F. Frank, *A Symposium on the Plastic Deformation of Crystalline Solids*: Mellon Institute, Pittsburgh, 19, 20 May 1950, Vol. 834, US Government Printing Office, 1950.
- [11] L. Priester, *Grain boundaries: from theory to engineering*, Vol. 172, Springer Science & Business Media, 2012.
- [12] W. T. Read, W. Shockley, *Dislocation models of crystal grain boundaries*, *Physical review* 78 (1950) 275.
- [13] P. Van Beers, V. Kouznetsova, M. Geers, M. Tschopp, D. McDowell, *A multiscale model of grain boundary structure and energy: From atomistics to a continuum description*, *Acta Materialia* 82 (2015).
- [14] S. Berbenni, B. Paliwal, M. Cherkaoui, *A micromechanics-based model for shear-coupled grain boundary migration in bicrystals*, *International Journal of Plasticity* 44 (2013).
- [15] V. Heinonen, C. Achim, K. Elder, S. Buyukdagli, T. Ala-Nissila, *Phase-field-crystal models and mechanical equilibrium*, *Physical Review E* 89 (2014).
- [16] J. Berry, N. Provatas, J. Rottler, C. W. Sinclair, *Phase field crystal modeling as a unified atomistic approach to defect dynamics*, *Physical Review B* 89 (2014).

- [17] Z. Trautt, A. Adland, A. Karma, Y. Mishin, Coupled motion of asymmetrical tilt grain boundaries: Molecular dynamics and phase field crystal simulations, *Acta Materialia* 60 (2012).
- [18] I. Beyerlein, A. Hunter, Understanding dislocation mechanics at the mesoscale using phase field dislocation dynamics, *Philosophical Transactions of the Royal Society A: Mathematical, Physical and Engineering Sciences* 374 (2016).
- [19] A. Acharya, A model of crystal plasticity based on the theory of continuously distributed dislocations, *Journal of the Mechanics and Physics of Solids* 49 (2001).
- [20] J. F. Nye, Some geometrical relations in dislocated crystals, *Acta metallurgica* 1 (1953).
- [21] E. Kröner, Continuum model of defects, *Physics of Defects*, Ed. R. Balian et al., North Holland, Amsterdam 218 (1980).
- [22] T. Mura, Continuous distribution of moving dislocations, *Philosophical Magazine* 8 (1963).
- [23] X. Zhang, A. Acharya, N. J. Walkington, J. Bielak, A single theory for some quasi-static, supersonic, atomic, and tectonic scale applications of dislocations, *Journal of the Mechanics and Physics of Solids* 84 (2015).
- [24] C. Fressengeas, V. Taupin, L. Capolungo, An elasto-plastic theory of dislocation and disclination fields, *International Journal of Solids and Structures* 48 (25-26) (2011) 3499–3509.
- [25] V. Taupin, L. Capolungo, C. Fressengeas, A. Das, M. Upadhyay, Grain boundary modeling using an elasto-plastic theory of dislocation and disclination fields, *Journal of the Mechanics and Physics of Solids* 61 (2013).
- [26] J. Guérolé, V. Taupin, M. Vallet, W. Yu, A. Guitton, Features of a nano-twist phase in the nanolayered Ti_3AlC_2 MAX phase, *Scripta Materialia* 210 (2022).
- [27] C. Fressengeas, V. Taupin, L. Capolungo, Continuous modeling of the structure of symmetric tilt boundaries, *International Journal of Solids and Structures* 51 (2014).
- [28] V. Taupin, L. Capolungo, C. Fressengeas, Disclination mediated plasticity in shear-coupled boundary migration, *International Journal of Plasticity* 53 (2014) 179–192.
- [29] S. Berbenni, V. Taupin, K. S. Djaka, C. Fressengeas, A numerical spectral approach for solving elasto-static field dislocation and g-disclination mechanics, *International Journal of Solids and Structures* 51 (2014).
- [30] K. S. Djaka, A. Villani, V. Taupin, L. Capolungo, S. Berbenni, Field dislocation mechanics for heterogeneous elastic materials: a numerical spectral approach, *Computer Methods in Applied Mechanics and Engineering* 315 (2017) 921–942.
- [31] D. Seif, G. Po, M. Mrovec, M. Lazar, C. Elsässer, P. Gumbsch, Atomistically enabled nonsingular anisotropic elastic representation of near-core dislocation stress fields in α -iron, *Physical Review B* (18) (2015) 184102.
- [32] C. Hartley, Y. Mishin, Characterization and visualization of the lattice misfit associated with dislocation cores, *Acta Materialia* 53 (5) (2005) 1313–1321.
- [33] G. Kresse, J. Hafner, Ab initio molecular dynamics for liquid metals, *Physical review B* 47 (1993).
- [34] B. Bienvenu, L. Dezerald, D. Rodney, E. Clouet, Ab initio informed yield criterion across body-centered cubic transition metals, *Acta Materialia* 236 (2022).
- [35] E. Clouet, B. Bienvenu, L. Dezerald, D. Rodney, Screw dislocations in BCC transition metals: from ab initio modeling to yield criterion, *Comptes Rendus. Physique* 22 (2021).
- [36] B. Bienvenu, C. C. Fu, E. Clouet, Impact of magnetism on screw dislocations in body-centered cubic chromium, *Acta Materialia* 200 (2020) 570–580.
- [37] A. P. Thompson, H. M. Aktulga, R. Berger, D. S. Bolintineanu, W. M. Brown, P. S. Crozier, P. J. in't Veld, A. Kohlmeyer, S. G. Moore, T. D. Nguyen, et al., LAMMPS—a flexible simulation tool for particle-based materials modeling at the atomic, meso, and continuum scales, *Computer Physics Communications* 271 (2022).
- [38] Y. Mishin, M. Mehl, D. Papaconstantopoulos, A. Voter, J. Kress, Structural stability and lattice defects in copper: Ab initio, tight-binding, and embedded-atom calculations, *Physical Review B* 63 (22) (2001) 224106.
- [39] M. A. Tschopp, S. P. Coleman, D. L. McDowell, Symmetric and asymmetric tilt grain boundary structure and energy in cu and al (and transferability to other fcc metals), *Integrating Materials and Manufacturing Innovation* 4 (2015) 176–189.
- [40] K. Djaka, V. Taupin, S. Berbenni, C. Fressengeas, A numerical spectral approach to solve the dislocation density transport equation, *Modelling and Simulation in Materials Science and Engineering* 23 (2015).
- [41] Atomistic manipulation toolkit, <https://www.ctcms.nist.gov/potentials/atomman> (2023).
- [42] P. Hirel, Atomsk: A tool for manipulating and converting atomic data files, *Computer Physics Communications* 197 (2015).
- [43] A. Stukowski, Visualization and analysis of atomistic simulation data with OVITO—the Open Visualization Tool, *Modelling and simulation in materials science and engineering* 18 (2009).
- [44] H. Grimmer, A reciprocity relation between the coincidence site lattice and the DSC lattice, *Scripta Metallurgica* 8 (1974).
- [45] I. S. Winter, T. Oettel, T. Frolov, R. Rudd, Characterization and visualization of grain boundary disconnections, *Acta Materialia* 237 (2022).
- [46] J. Guérolé, W. G. Nöhring, A. Vaid, F. Houllé, Z. Xie, A. Prakash, E. Bitzek, Assessment and optimization of the fast inertial relaxation engine (fire) for energy minimization in atomistic simulations and its implementation in lammps, *Computational Materials Science* 175 (2020) 109584.
- [47] S. Forest, N. Guéinchault, Inspection of free energy functions in gradient crystal plasticity, *Acta Mechanica Sinica* 29 (2013).

Supplementary Materials to:
Atomistic to continuum mechanics description of crystal defects with dislocation
density fields: application to dislocations and grain boundaries

Houssam Kharouji^a, Lucile Dezerald^b, Pierre Hirel^c, Philippe Carrez^c, Patrick Cordier^c, Vincent Taupin^a, Julien Guénolé^a

^aUniversité de Lorraine, CNRS, Arts et Métiers, LEM3, Metz, France

^bUniversité de Lorraine, CNRS, Institut Jean Lamour, Nancy, France

^cUniversité de Lille, CNRS, INRAE, Centrale Lille, UMET, Lille, France

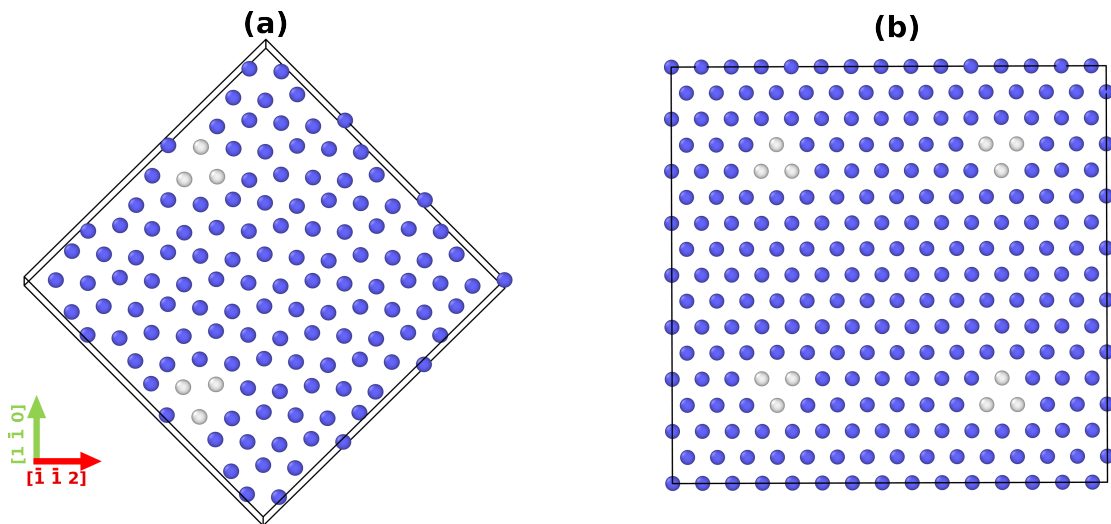


Figure S1: Tungsten simulation cells. Color coding is based on the common neighbor analysis [1]: blue, bcc; white, undefined environment. (a) Visualization of the screw dislocations dipole of opposite Burgers vectors in 135-atom simulation cell generated by DFT. (b) Quadruple of screw dislocations obtained through the periodic boundary conditions applied in all directions to the configuration depicted in (a). Rectangular crop is applied specifically for FFT calculations.

*Corresponding author

Email address: julien.guenole@univ-lorraine.fr (Julien Guénolé)

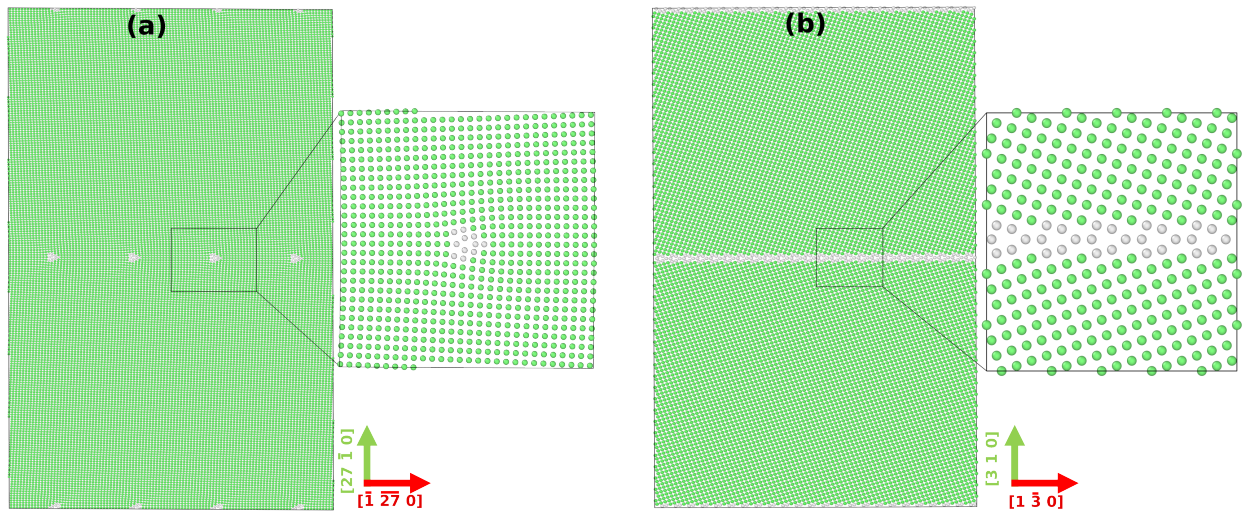


Figure S2: Snapshots of the atomistic simulation cells used for the grain boundaries calculations. Atoms are colored following the local structural type: green, FCC structure; white, undefined structure. a) Low angle grain boundary in copper. b) High angle grain boundary in copper

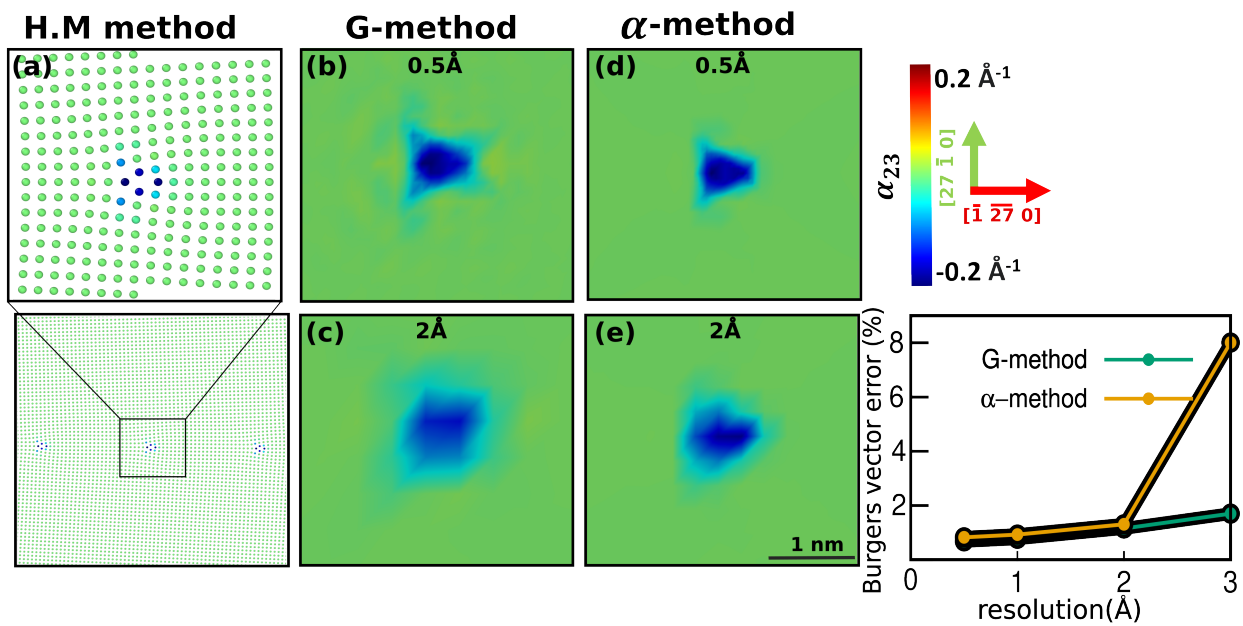


Figure S3: Edge dislocations within low angle grain boundary. Effect of FFT grid resolution on Nye dislocation density distributions and Burgers Vector norm error using G and α methods. (a) Visualization of the per-atom component α_{23} of the Nye tensor as obtained from the Hartley-Mishin method. (b) and (c): maps illustrating the edge dislocation density distribution obtained using the G-method with FFT Grid resolutions of 0.5 Å and 2 Å, respectively. (d) and (e) depict edge dislocation density distributions using the α method with 0.5 Å and 2 Å FFT grid resolutions. (f) The variation of the Burgers vector norm error as a function of the grid resolution using the G-method (Green line) and α method (Yellow line).

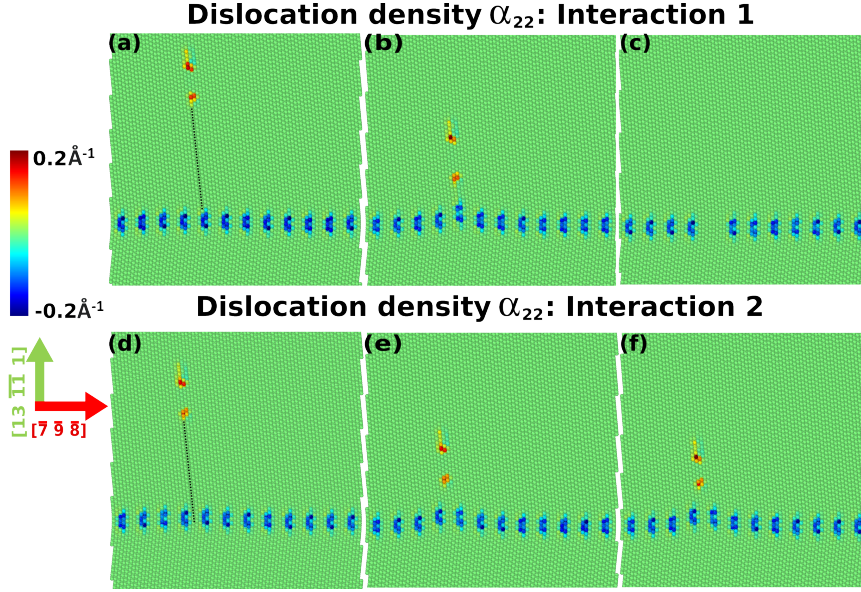


Figure S4: Interaction between extrinsic edge dislocation and $\Sigma 291(13 \bar{1} 1)[\bar{1} \bar{1} 2]$ STGB in copper: Visualization of the per-atom α_{23} Nye density during molecular static minimization. The GB is created initially by rotating two crystal lattices oriented along the x[1 $\bar{1}$ 0], y[1 1 1], and z[$\bar{1}$ $\bar{1}$ 2] directions around the z-axis by angles of $\theta/2 = 5.83^\circ$ and $-\theta/2 = 5.83^\circ$, respectively. An energy minimization is performed, using the FIRE algorithm [2], to obtain the grain boundary relaxed structure. The edge dislocation line is aligned parallel to the z-axis. The Burgers vector is set at $b = 2.55 \text{ \AA}$ within a (1 1 1) plane. (a, b, d, e) depicting the dislocation density distribution in unstable configurations, observed when the norm of the global force vector f_c exceeds 10^{-6} eV/\AA . (c, f) illustrates the relaxed configuration with a global force vector norm below f_c .

Figure S7 illustrates the influence of the interpolation methods on the Nye density distribution. It is worth important to notice that interpolation serves to transfer data onto the FFT grid. The examined interpolation modes here include linear, cubic, and nearest methods. Fig (S7.b) depicts the linear method, where the interpolation is performed by triangulating the component of the per-atom transformation tensor, followed by linear barycentric interpolation on each triangle. As depicted in Figure (S7.b), this mode effectively captures the threefold symmetry of the screw dislocation core. In Figure (S7.c), we depict the cubic method. Interpolation is achieved by triangulating the per-atom data and then constructing a cubic interpolating polynomial on each triangle using a Clough-Tocher scheme [3, 4]. Essentially, we connect points (x_i, y_i) and (x_{i+1}, y_{i+1}) are connected with a cubic polynomial $S_i(x) = a_i x^3 + b_i x^2 + c_i x + d_i$. To determine the interpolating function, it is necessary find the coefficients a_i, b_i, c_i, d_i for each of the cubic functions. Despite this method provides a general trend, linear interpolation effectively captures the symmetry of the screw core. In the last case we assessed the nearest interpolation method. In this technique, the interpolated pixel adopts the value of the nearest known pixel. This method provides the least accurate Nye distribution information (see figure (S7.d)). Similarly, we evaluated the influence of the interpolation method on the profiles of the elastic strain ϵ_{23} along the [$\bar{1}$ $\bar{1}$ 2] direction obtained with the G method. In the figure, we compare the shear strain profiles using the three aforementioned interpolation methods. Once again, the linear interpolation method accurately captures the elastic strain both near and away from the core region, providing results comparable to the elastic strain calculated using the Hartley and Mishin algorithm.

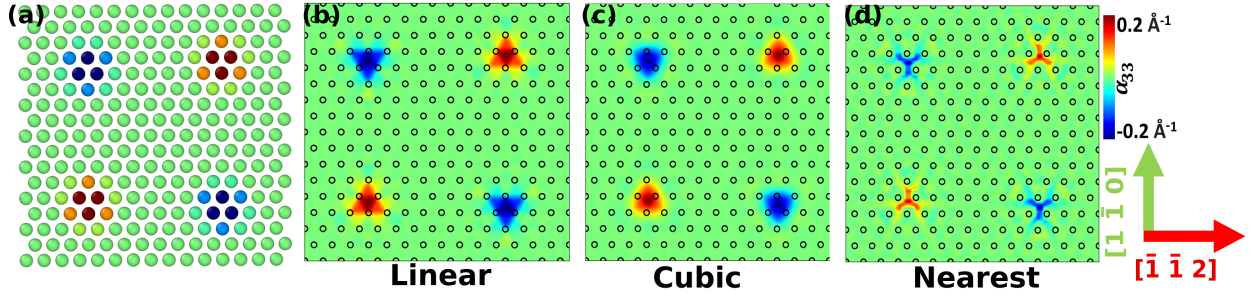


Figure S5: Effect of the interpolation methods on the Nye density distribution of screw dislocation quadruple in tungsten. (a) Visualization of the per-atom α_{33} Nye. Maps illustrating α_{33} Nye distribution using the G method and 0.5 Å FFT grid resolution. (a) linear, (b) cubic, and (c) nearest interpolation

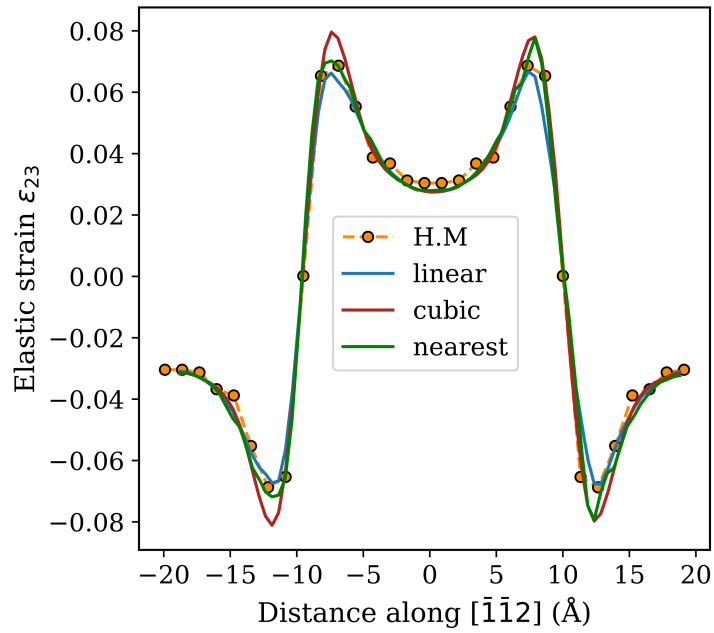


Figure S6: Effect of the interpolation methods on the elastic strain field obtained with the G method for screw dislocation in tungsten using a 0.5 Å FFT grid resolution and compared to the HM method atomistic results.

Table 1: Calculation time as a function of FFT grid resolutions across the different steps of the G method

Systems	Atomistic	Interpolation		FDM
	CPU time	Δx	CPU time	CPU time
Screw dislocation dipole in W	2.41h on 1024 cores	0.5 Å	0.14s on 1 core	0.987s on 1 core
		1.0 Å	0.09s on 1 core	0.280s on 1 core
		2.0 Å	0.05s on 1 core	0.079s on 1 core
		3.0 Å	0.04s on 1 core	0.039s on 1 core
LAGB in copper	24min on 64 cores	0.5 Å	8.66s on 1 core	51.71s on 1 core
		1.0 Å	3.57s on 1 core	13.50s on 1 core
		2.0 Å	2.34s on 1 core	3.713s on 1 core
		3.0 Å	2.05s on 1 core	1.710s on 1 core
HAGB in copper	15.2min on 64 cores	0.5 Å	2.67s on 1 core	16.35s on 1 core
		1.0 Å	1.14s on 1 core	4.140s on 1 core
		2.0 Å	0.76s on 1 core	1.101s on 1 core
		3.0 Å	0.55s on 1 core	0.491s on 1 core

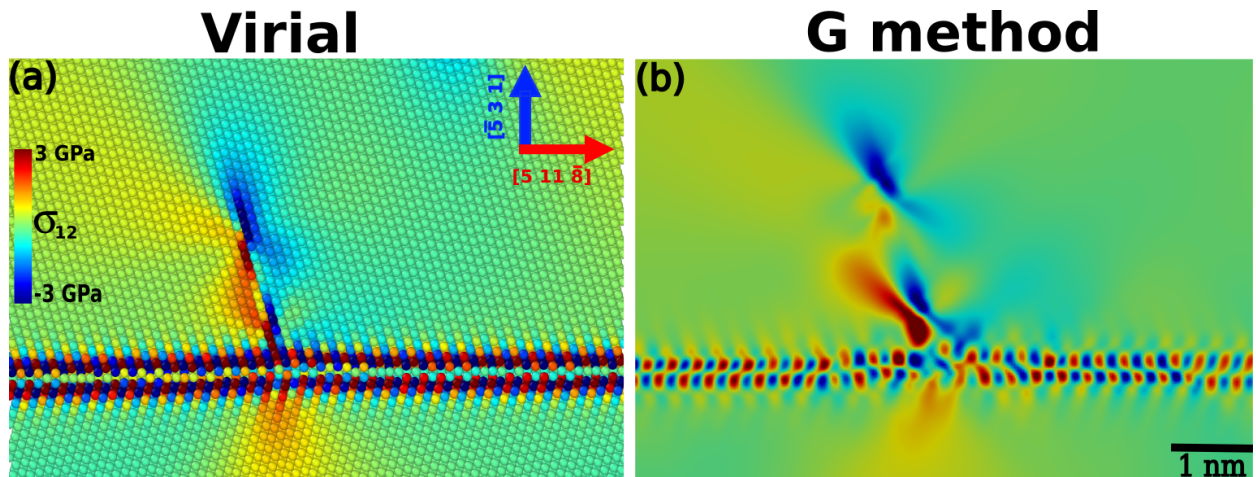


Figure S7: Interaction between an extrinsic edge dislocation and a $\Sigma 35(\bar{5}31)[112]34.05^\circ$ high angle STGB in copper. (a) Visualization of the per-atom Virial stress σ_{12} . (b) Maps illustrating elastic stress field σ_{12} obtained using the G method for 0.5 Å FFT grid resolution

References

- [1] A. Stukowski, Visualization and analysis of atomistic simulation data with OVITO—the Open Visualization Tool, *Modelling and simulation in materials science and engineering* 18 (2009).
- [2] J. Guérolé, W. G. Nöhring, A. Vaid, F. Houllé, Z. Xie, A. Prakash, E. Bitzek, Assessment and optimization of the fast inertial relaxation engine (fire) for energy minimization in atomistic simulations and its implementation in lammps, *Computational Materials Science* 175 (2020) 109584.
- [3] P. Alfeld, A trivariate clough tocher scheme for tetrahedral data, *Computer Aided Geometric Design* 1 (2) (1984) 169–181.
- [4] G. Farin, Triangular bernstein bezier patches, *Computer Aided Geometric Design* 3 (2) (1986) 83–127.